ACS APPLIED MATERIALS & INTERFACES

Research Article

www.acsami.org

Creation of $Cu_2O@TiO_2$ Composite Photocatalysts with *p*–*n* Heterojunctions Formed on Exposed Cu_2O Facets, Their Energy Band Alignment Study, and Their Enhanced Photocatalytic Activity under Illumination with Visible Light

Lingmei Liu,[†] Weiyi Yang,[†] Wuzhu Sun,[†] Qi Li,*[,†] and Jian Ku Shang[†,‡]

[†]Environment Functional Materials Division, Shenyang National Laboratory for Materials Science, Institute of Metal Research, Chinese Academy of Sciences, Shenyang 110016, China

[‡]Department of Materials Science and Engineering, University of Illinois at Urbana–Champaign, Urbana, Illinois 61801, United States

ABSTRACT: The creation of photocatalysts with controlled facets has become an important approach to enhance their activity. However, how the formation of heterojunctions on exposed facets could affect their photocatalytic performance ranking had not yet been investigated. In this study, $Cu_2O@TiO_2$ core–shell structures were created, and Cu_2O/TiO_2 *p*–*n* heterojunctions were formed on various exposed facets of Cu_2O cubes, Cu_2O cuboctahedra, and Cu_2O octahedra, respectively. These $Cu_2O@TiO_2$ polyhedra demonstrated an enhanced photocatalytic degradation effect on Methylene Blue (MB) and 4-nitrophenol (4-NP) under visible light illumination, because of the enhanced charge carrier separation by the formation of $Cu_2O@TiO_2$ *p*–*n* heterojunctions. It was further found that their photocatalytic performance was also facet-dependent as pure Cu_2O polyhedra, while the photocatalytic performance ranking of these $Cu_2O@TiO_2$ polyhedra was different with that of their corresponding Cu_2O polyhedron cores. By the combination of optical property measurement and XPS analysis, the energy band alignments of these $Cu_2O@TiO_2$ polyhedra were determined, which demonstrated that $Cu_2O@TiO_2$ octahedra had the highest band offset for the separation of charge carriers. Thus, the charge-carrier-separation-driven force in $Cu_2O@TiO_2$ polyhedra was different from their corresponding Cu_2O polyhedron cores, which resulted in their different surface photovoltage spectrum (SPS) responses and different photocatalytic performance rankings.

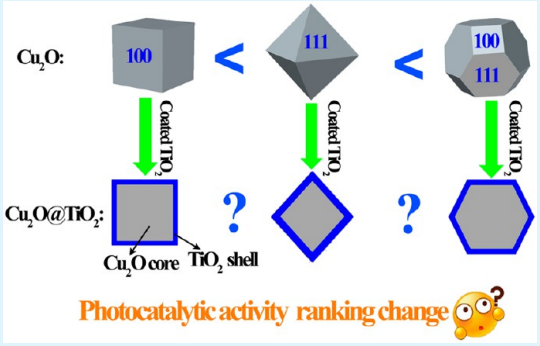

KEYWORDS: *$Cu_2O@TiO_2$ polyhedra, exposed facets, p-n heterojunctions, energy band alignment, visible light photocatalytic activity*

1. INTRODUCTION

Over the past few decades, semiconductor-based photocatalysts have attracted considerable research attention for both solar energy conversion and environmental applications.[1−4] Compared with single-phase semiconductor photocatalysts, composite photocatalysts with heterojunctions could possess greatly enhanced photocatalytic activities when properly designed, because the band level differences and inner electrostatic field in the heterojunction could provide the driving force for the separation of photogenerated electrons and holes.[5,6] Heterogeneous photocatalysts could also have different light response ranges, which may extend the light absorption of composite photocatalysts and enhance their solar efficiency.[7,8] Currently, most reported composite photocatalysts with heterojunctions did not have controlled facets,[9−11] while the development of photocatalysts with controlled facets has become an important approach to obtain photocatalysts with higher activity, since the first report by Lu and co-workers on the synthesis of anatase TiO_2 sheets with 47% exposed {001} facets in 2008.[12−15]

Early work demonstrated that photocatalysts with exposed facets of higher surface energy were more active than their counterparts with thermodynamically stable facets.[16,17] Recently, it was found that their photocatalytic activity could be further enhanced by incorporating different exposed facets and optimizing the ratio.[18,19] Because of the slight surface energy difference of the valence and conduction bands between different facets, photogenerated electrons and holes could be driven to different facets, leading to better charge carrier separation and the subsequently enhanced photocatalytic performance.[20−22] Thus, it is of interest to develop composite photocatalysts with heterojunctions formed on controlled facets, which could provide a stronger driving force for the enhanced charge carrier separation than corresponding single-phase photocatalysts with exposed facets, because of the larger differences in band energy from the formation of hetero-

Received: August 29, 2014
Accepted: December 29, 2014
Published: December 29, 2014

DOI: 10.1021/am505861c
ACS Appl. Mater. Interfaces 2015, 7, 1465−1476

junctions. Furthermore, the creation of heterojunctions on exposed facets of photocatalysts may also change their photocatalytic performance ranking, because the driving force for the charge carrier separation now relies on the different band alignments from heterojunctions constructed on different facets, not the slight difference in surface energy of the valence and conduction bands between different facets.

Cuprous oxide (Cu_2O), which is a *p*-type semiconductor with a direct band of 2.17 eV, is an ideal candidate for the study of the facet-dependent photocatalytic properties, because it is relatively easy to create Cu_2O crystals with controlled shapes and facets. Cu_2O crystals with various morphologies had been successfully synthesized, including nanowires, spheres, cubes, octahedra, cuboctahedra, truncated octahedra, dodecahedra, 26-facet polyhedra, 50-facet polyhedra, and so on.[23,24] Among them, Cu_2O crystals with cubic and octahedral geometries are the most important, because more-complex structures could be derived from them, and their well-defined facets provide unique opportunities for the examination of their facet-dependent properties.[25,26] Cu_2O/TiO_2 composite photocatalysts with heterojunctions had been developed, which demonstrated enhanced photocatalytic activities, compared with pure Cu_2O, because of the improved charge carrier separation from the *p*−*n* heterojunction effect.[27,28] However, most of these Cu_2O/TiO_2 composite photocatalysts were created without well-defined facets and the band alignments and photocatalytic activities of Cu_2O/TiO_2 composite photocatalysts with well-defined facets had not been investigated.[29,30]

In this work, $Cu_2O@TiO_2$ core−shell structures were created by a facile hydrothermal process to create an anatase TiO_2 coating shell onto three types of Cu_2O crystal cores, namely, Cu_2O cubes with exposed {100} facets, Cu_2O cuboctahedra with exposed {100} and {111} facets, and Cu_2O octahedra with exposed {111} facets, respectively. Thus, Cu_2O/TiO_2 *p*−*n* heterojunctions were formed on different exposed facets of Cu_2O, and these $Cu_2O@TiO_2$ polyhedra also exhibited a facet-dependent photocatalytic performance on the degradation of Methylene Blue (MB) and 4-nitrophenol (4-NP) under visible light illumination as their counterparts with no TiO_2 shells. Interestingly, it was found that the photocatalytic performance ranking of these $Cu_2O@TiO_2$ polyhedra was different with that of their corresponding Cu_2O polyhedron cores. The investigation on band alignments of these $Cu_2O@TiO_2$ polyhedra demonstrated that the band offset at the heterojunction interface was also facet-dependent, which provided the major driving force for the separation of photogenerated electrons and holes. The separation process was different, compared with Cu_2O polyhedra with exposed facets. Thus, it is not appropriate to assume that a photocatalyst with the favorite exposed facets will still demonstrate the best photocatalytic performance when heterojunctions formed on its exposed facets.

2. EXPERIMENTAL SECTION

2.1. Chemicals and Materials. Copper(II) chloride dihydrate ($CuCl_2{\cdot}2H_2O$, 99%, Sinopharm Chemical Reagent Co., Ltd., Shanghai, PRC) was used as the Cu source, polyvinylpyrrolidone (PVP k30, Sinopharm Chemical Reagent Co., Ltd., Shanghai, PRC) was used as the surfactant, sodium hydroxide (NaOH, 96%, Sinopharm Chemical Reagent Co., Ltd., Shanghai, PRC) was used as the precipitation reagent, and L-ascorbic acid (99.7%, Kemiou Chemicals Co. Ltd., Tianjin, PRC) was used as the reducing agent in the synthesis of Cu_2O polyhedra, respectively. Deionized (DI) water was used as the solvent in this process. Titanic fluoride (TiF_4, 98%, J&K Chemical Ltd., Shanghai, PRC) was used as the Ti source and ethyl alcohol (EtOH, 99.7%, Sinopharm Chemical Reagent Co., Ltd., Shanghai, PRC) was used to wash the products. Methylene Blue (MB, Kemiou Chemicals Co. Ltd., Tianjin, PRC) and 4-nitrophenol (4-NP, 99%, Alfa Aesar Chemical Ltd., Tianjin, PRC) were used as the target compounds to investigate the visible-light-induced photocatalytic activities of samples.

2.2. Synthesis of Cu_2O Nanocrystals. The Cu_2O nanocrystals were synthesized by a modified method, according to a reported process.[31] In a typical experiment, given amounts of PVP (0.556 g for cubes, 3.3 g for cuboctahedra, 8.8 g for octahedra) and 0.1 g sodium citrate was first dissolved in 100 mL of DI water, and 0.171 g of $CuCl_2{\cdot}2H_2O$ was added into the above solution. Then, 10 mL NaOH aqueous solution (2 M) was added dropwise (1 drop/s) into the above mixture solution with continuous stirring for 0.5 h. Finally, 10 mL of L-ascorbic acid aqueous solution (0.6 M) was added dropwise and the mixture was aged for 3 h before being centrifuged at 9000 rpm for 5 min. All of these procedures were carried out in a water bath at 55 °C. The obtained precipitates were washed with excessive DI water and EtOH for several times to remove unreacted chemicals and PVP surfactants, and then dried in vacuum at 50 °C for 10 h to obtain desired Cu_2O nanocrystals for further characterization and use.

2.3. Preparation of $Cu_2O@TiO_2$ Core−Shell Polyhedra. A quantity of 0.01 g of obtained Cu_2O crystals was dispersed in 25 mL of DI water with the aid of ultrasonication for 10 min. Then, 0.4 mL of TiF_4 aqueous solution (0.02 M) was slowly added dropwise into the Cu_2O suspension and stirred for 1 h. After thorough mixing, the suspension was transferred into a 50 mL Teflon-lined stainless steel autoclave and heated at 180 °C for 0.5 h in an oven. After the reaction, the products were collected, went through several rinse-centrifugation cycles with DI water and EtOH separately, and then dried at 60 °C for 10 h in a vacuum oven. Pure anatase TiO_2 nanoparticles were prepared by the same procedure without the addition of Cu_2O crystals.

2.4. Material Characterization. The crystal structures of samples were analyzed by X-ray diffraction (XRD) on a Model D/MAX-2004 powder X-ray diffractometer (Rigaku Corporation, Tokyo, Japan) with Ni-filtered Cu Kα radiation (λ = 1.54178 Å) at 56 kV and 182 mA. The morphologies of samples were observed using field-emission scanning electron microscopy (FESEM) and transmission electron microscopy (TEM). FESEM observations were conducted by a Model SUPRA55 SEM system (Zeiss, Germany). TEM observations were conducted on a Model 2100 TEM system (JEOL, Ltd., Tokyo, Japan) operated at 200 kV with a point-to-point resolution of 0.28 nm, and TEM samples were prepared by dispersing a thin film of these powder samples on Ni grids. Brunauer−Emmett−Teller (BET) measurement was conducted by N_2 adsorption−desorption isotherm with an Autosorb-1 Series Surface Area and Pore Size Analyzers (TriStar II 3020, Micromeritics Instrument Corporation, USA). The ultraviolet−visible light (UV-vis) spectra of samples were measured on a UV-2550 spectrophotometer (Shimadzu Corporation, Kyoto, Japan). X-ray photoelectron spectroscopy (XPS) measurements were conducted using a Model ESCALAB 250 X-ray photoelectron spectrometer (Thermo Fisher Scientific Inc., Waltham, MA, USA) with an Al Kα anode (1486.6 eV photon energy, 300 W). The surface photovoltage spectra (SPS) of samples were measured with a home-built apparatus that had been described in detail elsewhere.[32]

2.5. Photocatalytic Degradation of Methylene Blue and 4-Nitrophenol under Visible-Light Illumination. MB was used as a model organic pollutant to evaluate the photocatalytic activity of samples under visible-light illumination. A quantity of 0.01 g of photocatalyst was dispersed in 25 mL of DI water in a 150-mL glass beaker via ultrasonication for 10 min, followed by the addition of 25 mL of a 2×10^{-5} M aqueous MB solution. Thus, the initial concentration of MB was 1×10^{-5} M, and a fixed concentration of 0.2 mg photocatalyst/mL solution was used. A 300-W xenon lamp (PLS-SXE300, Beijing Perfect Light Technology Co., Ltd., Beijing, PRC) was used as the light source, which had a glass filter to provide zero light intensity below 400 nm. The light intensity striking the MB solution was at ca. 23 mW/cm^2, as measured by a Model FZ-A optical radiometer (Photoelectric Instrument Factory, Beijing Norman University, Beijing, PRC). During the photocatalytic treatment, the suspension was under continuous magnetic stirring. At each time

DOI: 10.1021/am505861c
ACS Appl. Mater. Interfaces 2015, 7, 1465−1476

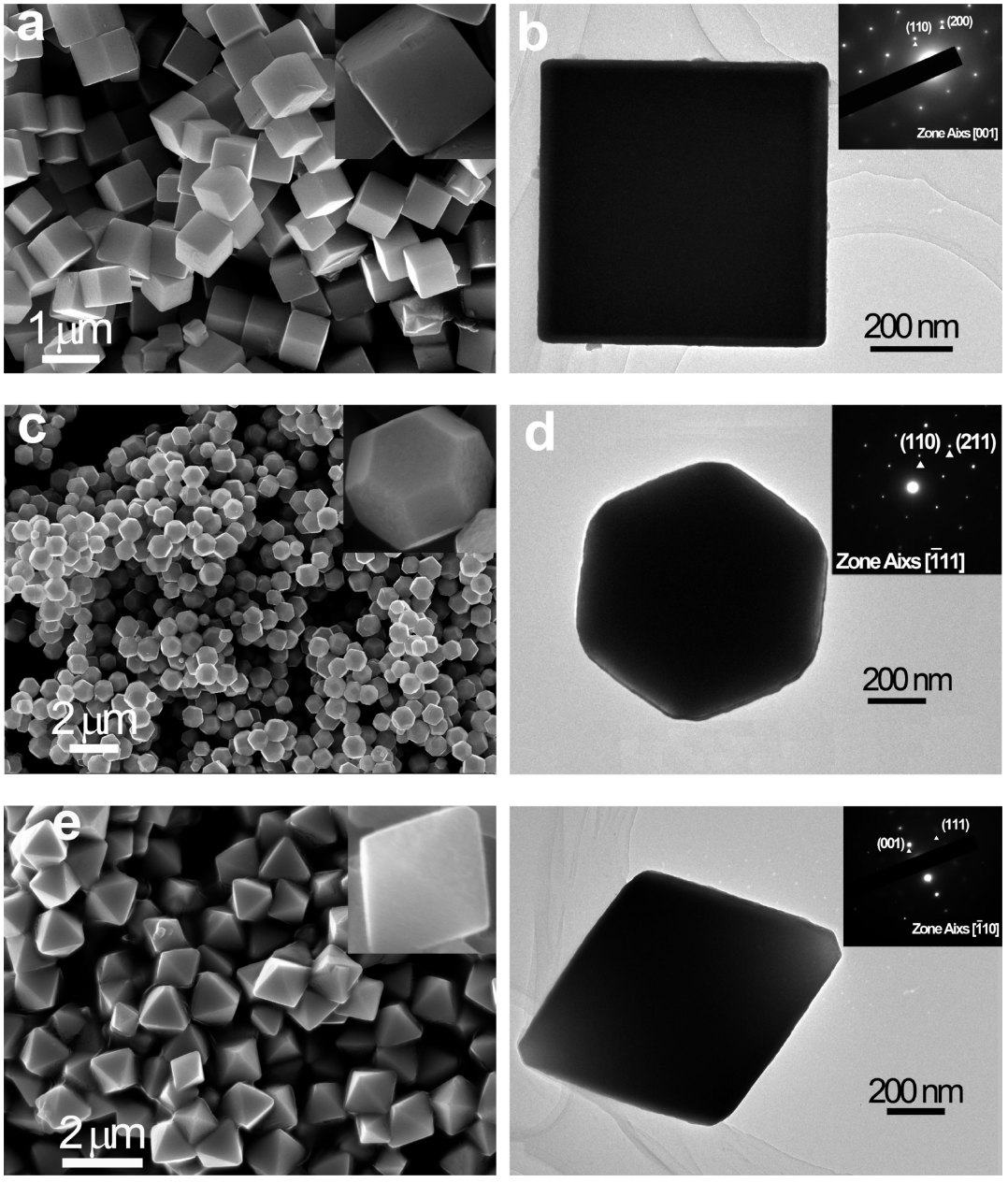

Figure 1. SEM and TEM images of Cu_2O cubes (panels (a) and (b)), cuboctahedra (panels (c) and (d)), and octahedra (panels (e) and (f)). The inset shown in the upper right-hand corner of each SEM image shows the samples at a higher magnification, and the insets shown in the upper right-hand corner in the TEM images show the corresponding selected area electron diffraction (SAED) patterns.

interval, photocatalysts were separated by centrifugation at 10 500 rpm for 5 min, and the MB concentration of the clear solution was measured by the Model UV-2550 spectrophotometer that was monitoring the absorption maximum at λ_{max} = 664 nm. All analyses were performed in triplicate. 4-NP is a toxic organic pollutant that does not absorb visible light, and it is difficult to be photodegraded.[33] For its photocatalytic degradation experiment, 0.02 g of photocatalyst was dispersed in 50 mL of 4-NP solution (10 mg/L). The residual 4-NP concentration in the treated solution was measured by the Model UV-2550 spectrophotometer monitoring the absorption maximum at λ_{max} = 317 nm. Other procedures were similar as those used in the MB photocatalytic degradation experiment.

3. RESULTS AND DISCUSSION

3.1. The Morphologies and Crystal Structures of Cu_2O Crystals with Well-Defined Facets. Cu_2O crystals with well-defined facets were synthesized by reducing a copper citrate complex solution with ascorbic acid in the presence of polyvinylpyrrolidone (PVP). It had been reported by Zhang et al. that {111} planes of Cu_2O selectively adsorbed PVP during the crystal growth process, which could stabilize the {111} plane and thus hinder the growth rate perpendicular to it.[31] Thus, Cu_2O crystals with different {100} to {111} ratios could be synthesized by a simple modulation of the PVP amount in this synthesis process. As demonstrated in Figure 1, Cu_2O cubes, cuboctahedra, and octahedra were successfully synthesized based on this approach, and they all had smooth surfaces. Figure 1a shows the SEM image of Cu_2O cubes, and the inset in Figure 1a shows one Cu_2O cube at a higher magnification. The average edge length of these Cu_2O cubes was ~700 nm, and all the six exposed surfaces of the cubes were made of six {100} facets. Figure 1b shows the TEM image of

DOI: 10.1021/am505861c
ACS Appl. Mater. Interfaces 2015, 7, 1465−1476

one Cu_2O cube, and the inset in Figure 1b shows the corresponding selected area electron diffraction (SAED) pattern. The electron beam was aligned along the [001] direction; a two-dimensional square could be observed in Figure 1b, and the inset SAED pattern demonstrated that the Cu_2O cube was a single crystal. Figure 1c shows the SEM image of cuboctahedra, and the inset in Figure 1c shows one Cu_2O cuboctahedron with a higher magnification. The average edge length of these Cu_2O cuboctahedra was ~400 nm, and the exposed surfaces of the cuboctahedra were made of six {100} facets and eight {111} facets. Figure 1d shows the TEM image of one Cu_2O cuboctahedron, and the inset in Figure 1d shows the corresponding SAED pattern. The electron beam was aligned along the [$\bar{1}$11] direction; a two-dimensional hexagon could be observed in Figure 1d, and the inset SAED pattern demonstrated that the Cu_2O cuboctahedron was a single crystal. Figure 1e shows the SEM image of Cu_2O octahedra, and the inset in Figure 1e shows one Cu_2O octahedron with a higher magnification. The average edge length of these Cu_2O octahedra was ~1 μm, and all the eight exposed surfaces of the octahedra were made of {111} facets. Figure 1f shows the TEM image of one Cu_2O octahedron, and the inset in Figure 1f shows the corresponding SAED pattern. The electron beam was aligned along the [$\bar{1}$10] direction; a two-dimensional rhombus could be observed in Figure 1f, and the inset SAED pattern demonstrated that the Cu_2O octahedron was a single crystal. Thus, the increase of PVP content in the reaction solution induced a shape evolution of Cu_2O crystals from cubes with all exposed surfaces of {100} facets to cuboctahedra with mixed exposed surfaces of {100} and {111} facets, and finally to octahedra with all exposed surfaces of {111} facets, corresponding to the gradual shrinkage of exposed {100} facets and enlargement of exposed {111} facets.

Figure 2 shows the X-ray diffraction (XRD) patterns of these Cu_2O crystals with well-controlled morphologies and exposed

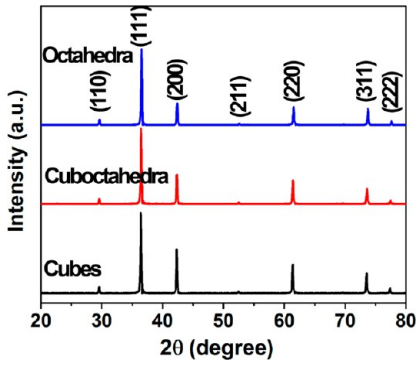

Figure 2. X-ray diffraction (XRD) patterns of Cu_2O cubes (black spectrum), cuboctahedra (red spectrum), and octahedra (blue spectrum).

facets. No diffraction peak of CuO or Cu could be found in their XRD patterns, and all diffraction peaks belonged to the face-centered cubic Cu_2O phase (Powder Diffraction File (PDF) Card No. 05-0667). The strong and sharp peaks indicated that all these Cu_2O crystals had a high degree of crystallinity. Although their XRD patterns were similar due to random particle orientations, a further examination demonstrated that the ratio of the intensity of the (200) peak to that of the (111) peak decreased gradually from 0.54 for Cu_2O cubes to 0.39 for Cu_2O cuboctahedra, and finally to 0.28 for Cu_2O octahedra, respectively. This trend was as expected because the fractions of {100} facets gradually decreased when the Cu_2O crystal shape changed from cubes to cuboctahedra, and finally to octahedra,[23] which was in agreement with the SEM and TEM observations.

3.2. The Morphologies and Crystal Structures of Cu_2O@TiO_2 Core–Shell Polyhedra. Cu_2O@TiO_2 core–shell polyhedra were synthesized by a hydrothermal process to create Cu_2O/TiO_2 p–n heterojunctions on different exposed facets of Cu_2O crystals. The uniform coating of TiO_2 on colloidal particles is a challenging task, because of the very high reactivity of most titanium precursors.[34] In our process, TiF_4 was used as the titanium precursor for the shell creation during the hydrothermal process, because of its relatively slow hydrolysis and subsequent moderate precipitation of TiO_2 onto accessible surfaces of Cu_2O polyhedra.[35] Furthermore, the easy crystallization of TiO_2 from the hydrolysis of TiF_4 could largely shorten the hydrothermal process time, which avoided the morphology change of Cu_2O cores to obtain Cu_2O@TiO_2 core–shell polyhedra with same shapes as Cu_2O cores. Thus, the selection of TiF_4 as the titanium precursor in our approach was critical to obtain well-defined Cu_2O@TiO_2 core–shell polyhedra.

Figure 3 shows the XRD patterns of these Cu_2O@TiO_2 core–shell polyhedra, which demonstrated clearly that Cu_2O

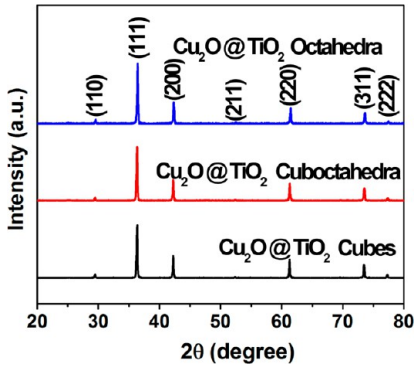

Figure 3. XRD patterns of Cu_2O@TiO_2 core–shell polyhedra (cubes (black spectrum), cuboctahedra (red spectrum), and octahedra (blue spectrum)).

cores were preserved well during the hydrothermal process. No diffraction peak of CuO or Cu could be found in their XRD patterns, and all diffraction peaks still belonged to the face-centered cubic Cu_2O phase (PDF Card No. 05-0667). No diffraction peak of TiO_2 could be found in these XRD patterns, which may be attributed to their low TiO_2 contents. Figure 4a shows the SEM image of Cu_2O@TiO_2 cubes, which demonstrated clearly that a uniform rough layer consisted of the aggregation of fine nanoparticles covered the smooth surface of Cu_2O cube and thus created core–shell structure had the same shape as that of the Cu_2O core. Figure 4b shows the TEM image of Cu_2O@TiO_2 cubes, which demonstrated that they had the square shape from the two-dimensional projection of cubes. The insert in Figure 4b shows the corresponding selected area electron diffraction (SAED) pattern on the cover shell as defined by the red square, which demonstrated that the shell was composed of well-crystallized anatase TiO_2. Figure 4c and 4d show the SEM and TEM image of Cu_2O@TiO_2 cuboctahedra, respectively, and Figure 4e and 4f show the SEM and TEM image of Cu_2O@TiO_2 octahedra, respectively.

DOI: 10.1021/am505861c
ACS Appl. Mater. Interfaces 2015, 7, 1465–1476

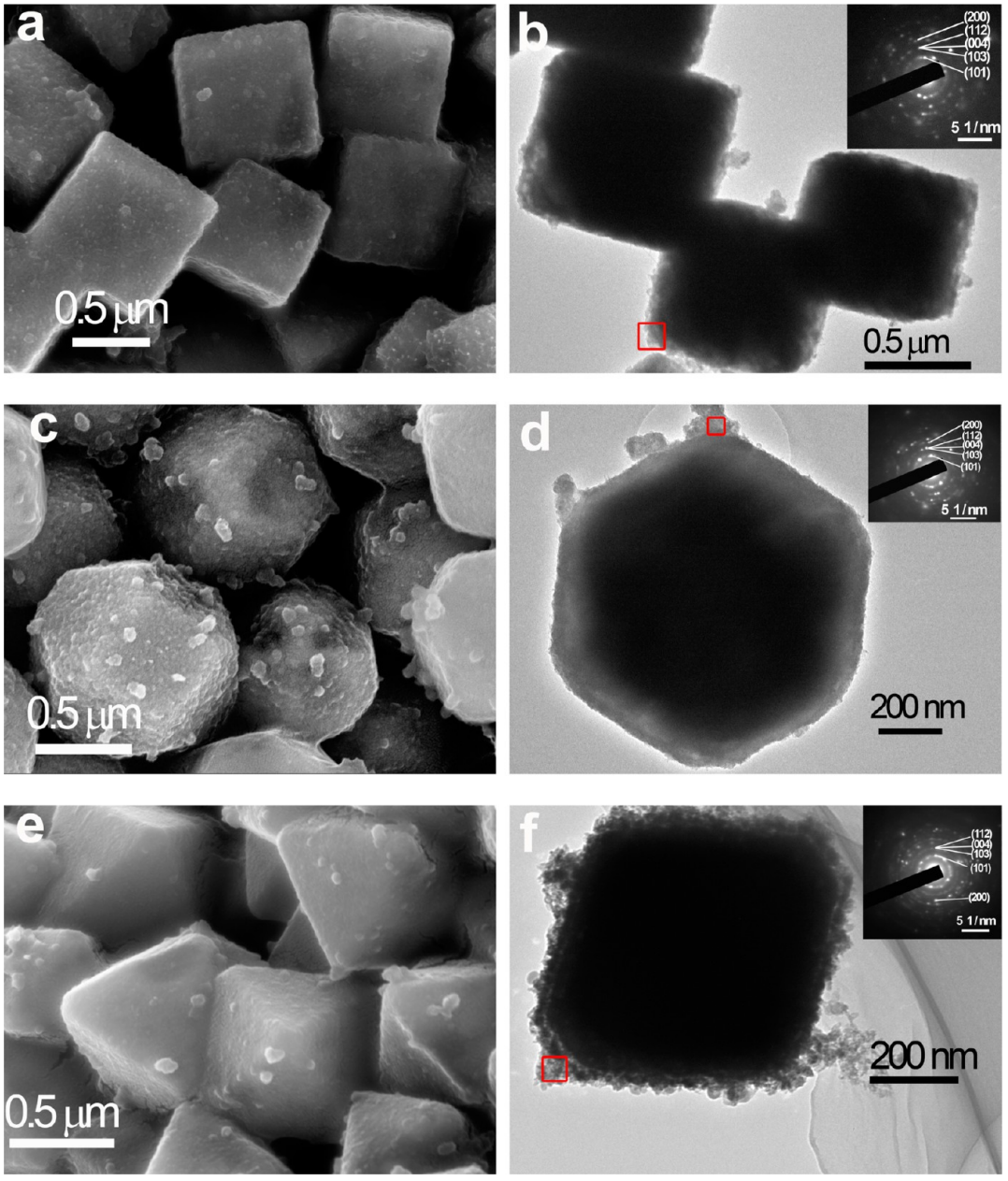

Figure 4. SEM and TEM images of $Cu_2O@TiO_2$ cubes (panels (a) and (b)), cuboctahedra (panels (c) and (d)), and octahedra (panels (e) and (f)). The inserts in TEM images show the corresponding SAED patterns on the cover shell regions defined by the red square.

Similar to that observed with $Cu_2O@TiO_2$ cubes, uniform rough layers that consisted of the aggregation of well-crystallized, fine TiO_2 nanoparticles covered the smooth surface of Cu_2O cuboctahedra and octahedral after the hydrothermal process, which created core−shell structures that had the same shapes as those of the Cu_2O cores. Thus, TiO_2/Cu_2O *n*−*p* heterojunctions were created on different exposed facets of Cu_2O crystals, which could have a large impact on their photocatalytic performance, as detailed in the following sections.

The contents of Ti in these $Cu_2O@TiO_2$ polyhedra were examined through SEM-EDS mapping, and results are summarized in Table 1. It was found that the contents of Ti in different $Cu_2O@TiO_2$ core−shell polyhedra were all ∼4 wt %, so the amounts of TiO_2 in different $Cu_2O@TiO_2$ polyhedra were similar. BET measurement results on these

Table 1. Content of Ti in Different $Cu_2O@TiO_2$ Core−Shell Polyhedra

	Ti (wt %)	Cu (wt %)
$Cu_2O@TiO_2$ cubes	3.95	96.05
$Cu_2O@TiO_2$ cuboctahedra	4.37	95.63
$Cu_2O@TiO_2$ octahedra	4.22	95.78

$Cu_2O@TiO_2$ polyhedra are summarized in Table 2. It clearly showed that these $Cu_2O@TiO_2$ polyhedra had very close BET specific surface area, pore volume, and average pore size values.

3.3. Optical Properties of Cu_2O Crystals with Well-Defined Facets and Anatase TiO_2 Nanoparticles. The optical properties of Cu_2O crystals with well-defined facets and anatase TiO_2 nanoparticles were investigated by measuring their diffuse reflectance spectra for the determination of band alignments in $Cu_2O@TiO_2$ core−shell polyhedra. From the

DOI: 10.1021/am505861c
ACS Appl. Mater. Interfaces 2015, 7, 1465−1476

Table 2. BET Surface Area, Pore Volume, And Average Pore Size for $Cu_2O@TiO_2$ Core−Shell Polyhedra

	BET specific surface area (m^2/g)	pore volume (cm^3/g)	average pore size (nm)
$Cu_2O@TiO_2$ cubes	4.27	0.026	24.6
$Cu_2O@TiO_2$ cuboctahedra	4.09	0.025	24.4
$Cu_2O@TiO_2$ octahedra	4.22	0.026	24.8

reflectance data, optical absorbance could be approximated by the Kubelka−Munk function, as given by eq 1:

$$F(R) = \frac{(1-R)^2}{2R} \quad (1)$$

where R is the diffuse reflectance.[36] Figure 5a shows the light absorbance (in term of Kubelka−Munk equivalent absorbance units) of Cu_2O cubes, Cu_2O cuboctahedra, and Cu_2O octahedra, compared with that of anatase TiO_2 nanoparticles. Anatase TiO_2 nanoparticles demonstrated the characteristic adsorption spectrum with the fundamental absorbance stopping edge at ~390 nm, most of their absorption was within the UV light region. All three Cu_2O crystals with well-defined facets, however, demonstrated much better light absorption in the visible-light region than anatase TiO_2 nanoparticles. Among them, Cu_2O octahedra had the highest visible-light absorption, while Cu_2O cubes had the lowest visible-light absorption.

The band gap values of these Cu_2O crystals with well-defined facets and anatase TiO_2 nanoparticles were determined by the construction of Tauc Plots ($(F(R)*h\nu)^n$ vs $h\nu$) from Figure 5a,[36] which were needed for the determination of the conduction band offset of $Cu_2O@TiO_2$ heterojunction.[37] Figure 5b shows Tauc Plots of these Cu_2O crystals with well-defined facets, and the inset in Figure 5b shows the Tauc Plot of anatase TiO_2 nanoparticles, respectively. As an indirect band gap semiconductor, n should be taken as 2 for Cu_2O.[38] Thus, the extrapolation of the linear region to the photon energy axis could yield bandgap values of these Cu_2O crystals with well-defined facets as 2.29 eV for Cu_2O cubes, 2.18 eV for Cu_2O cuboctahedra, and 2.05 eV for octahedra, consistent with their good visible-light absorption performances. The observed slight differences in their band-gap values could be attributed for their different morphologies as reported in the literature.[25] As a direct band-gap semiconductor, n should be taken as 0.5 for TiO_2.[39] Thus, the extrapolation of the linear region to the photon energy axis could yield the band-gap value of these anatase TiO_2 nanoparticles as 3.12 eV, which is consistent with their UV light absorption.

3.4. Energy Band Alignments at the Heterojunction Interface in $Cu_2O@TiO_2$ Core−Shell Polyhedra. The insight into the band alignments in $Cu_2O@TiO_2$ $p-n$ heterojunctions formed on different exposed facets of Cu_2O crystals was critical for the understanding of the photocatalytic performance differences among these $Cu_2O@TiO_2$ core−shell polyhedra. XPS studies were conducted on pure Cu_2O, pure TiO_2, and $Cu_2O@TiO_2$ samples, which is a well-documented technique for the determination of the valence band offset at heterojunction interfaces.[37,40,41] Although a simple estimation of the valence band offset could be made from the difference between the valence band maximum (VBM) of the two materials, it contains an appreciable error since the dipole is not taken into account in this simplified approach, which generally exists at the interface between the two materials.[40] To obtain a more accurate estimation of the valence band offset, the method proposed by Kraut et al. was applied in this study.[42] In this method, the energy difference between the core level (CL) and valence band maximum of the pure bulk materials, as well as the difference between the core levels at the heterojunction interface of the photocatalysts, were needed. The valence band offset (VBO), ΔE_{VBO}, of the $Cu_2O@TiO_2$ heterojunction could be calculated according to eq 2:

$$\Delta E_{VBO} = (E_{Cu,2p} - E_{V,Cu})^{Cu_2O}_{pure} - (E_{Ti,2p} - E_{V,Ti})^{TiO_2}_{pure} + \Delta E_{CL} \quad (2)$$

where

$$\Delta E_{CL} = (E_{Ti,2p} - E_{Cu,2p})^{Cu_2O@TiO_2}_{heterojunction} \quad (3)$$

The conduction band offset (CBO), ΔE_{CBO}, could be calculated according to eq 4:

$$\Delta E_{CBO} = E^{Cu_2O}_{gap} - E^{TiO_2}_{gap} + \Delta E_{VBO} \quad (4)$$

Figure 6 shows the XPS core-level and the valence band spectra for pure Cu_2O samples, pure TiO_2 samples, and $Cu_2O@TiO_2$ samples with heterojunctions. The circles shown in Figure 6 were the raw data points obtained from the XPS measurements, and the core-level spectra of various samples were then fitted with the combination of Gaussian and Lorentzian line shapes, together with a Shirley-typed background subtraction. The VBM positions in the VB spectra were

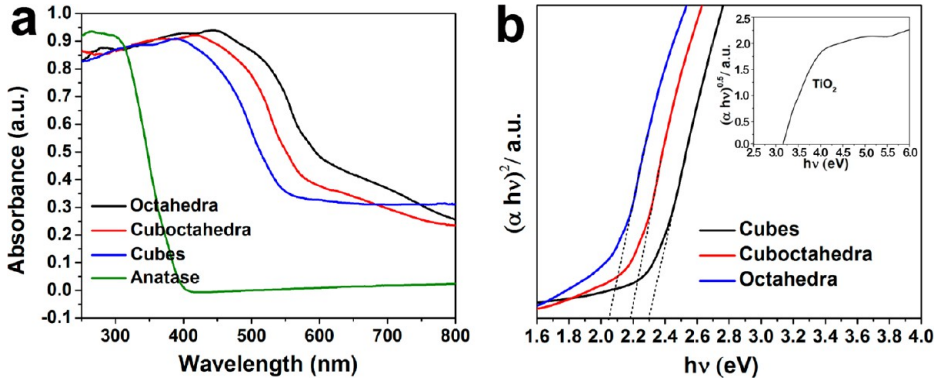

Figure 5. (a) UV-vis absorbance spectra of Cu_2O polyhedra, compared with that of anatase TiO_2 nanoparticles. (b) Tauc plots ($(F(R)*h\nu)^n$ vs $h\nu$) constructed from panel (a).

DOI: 10.1021/am505861c
ACS Appl. Mater. Interfaces 2015, 7, 1465−1476

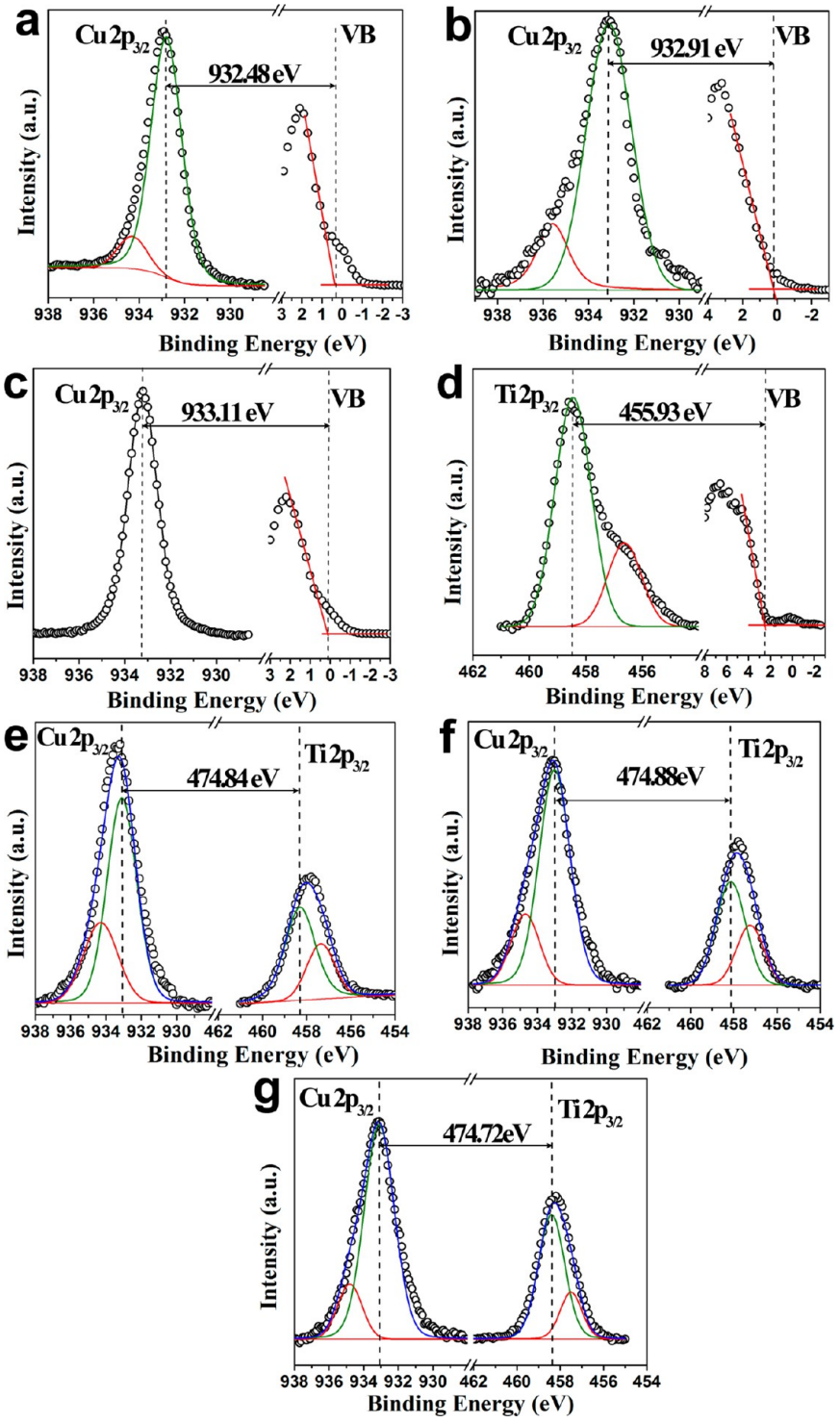

Figure 6. XPS core-level and valence band spectra obtained from (a) Cu_2O cubes, (b) Cu_2O cuboctahedra, (c) Cu_2O octahedra, (d) anatase TiO_2, (e) $Cu_2O@TiO_2$ cubes, (f) $Cu_2O@TiO_2$ cuboctahedra, and (g) $Cu_2O@TiO_2$ octahedra.

determined by the linear extrapolation of the leading edges of the VB spectra of the pure Cu_2O and TiO_2 samples with the baseline. Figures 6a, 6b, 6c, and 6d show the XPS core-level data for pure Cu_2O cubes, Cu_2O cuboctahedra, Cu_2O octahedra, and anatase TiO_2 nanoparticles, respectively, while Figures 6e, 6f, and 6g show the XPS core-level data for $Cu_2O@TiO_2$ cubes, $Cu_2O@TiO_2$ cuboctahedra, and $Cu_2O@TiO_2$ octahedra, respectively. From these data, the binding energy values for the core-level, VBM, and band-gap energy of pure Cu_2O samples, pure TiO_2 samples, and $Cu_2O@TiO_2$ samples with heterojunctions could be calculated, which were summarized in Table 3. Then, the VBO and CBO values for $Cu_2O@TiO_2$ core−shell polyhedra could be calculated from eqs 2−4, which were summarized in Table 4. Thus, the energy band alignment diagrams for $Cu_2O@TiO_2$ core−shell polyhedra could be constructed based on these calculation results, which were demonstrated in Figures 7a, 7b, and 7c for $Cu_2O@$

DOI: 10.1021/am505861c
ACS Appl. Mater. Interfaces 2015, 7, 1465−1476

Table 3. Binding Energy Values for the Core-Level, VBM, and the Band-Gap Energy for Pure Cu_2O Samples, Pure TiO_2 Samples, and Cu_2O@TiO_2 Samples with Heterojunctions[a]

	Cubic-Cu_2O	Cubo-Cu_2O	Octa-Cu_2O	TiO_2	Cubic-CT	Cubo-CT	Octa-CT
Cu $2p_{3/2}$ (eV)	932.81	933.12	933.23		933.15	933.01	933.06
Ti $2p_{3/2}$ (eV)				458.47	458.31	458.13	458.34
VBM (eV)	0.33	0.21	0.12	2.54			
E_{gap} (eV)	2.29	2.181	2.047	3.12			

[a]Table legend: Cubic-Cu_2O, Cu_2O cubes; Cubo-Cu_2O, Cu_2O cuboctahedra; Octa-Cu_2O, Cu_2O octahedra; Cubic-CT, Cu_2O@TiO_2 cubes; Cubo-CT, Cu_2O@TiO_2 cuboctahedra; and Octa-CT, Cu_2O@TiO_2 octahedra.

Table 4. VBO and CBO Values for Cu_2O@TiO_2 Core−Shell Polyhedra

	VBO (eV)	CBO (eV)
Cu_2O@TiO_2 cubes	1.71	0.88
Cu_2O@TiO_2 cuboctahedra	2.10	1.16
Cu_2O@TiO_2 octahedra	2.46	1.39

TiO_2 cubes, Cu_2O@TiO_2 cuboctahedra, and Cu_2O@TiO_2 octahedra, respectively.

These Cu_2O@TiO_2 core−shell polyhedra had different band offset values, which demonstrated a clear facet dependency. Cu_2O@TiO_2 octahedra had the highest band offset value and Cu_2O@TiO_2 cuboctahedra had the medium band offset value, while Cu_2O@TiO_2 cubes had the lowest band offset value. Upon illumination with visible light, only the Cu_2O core could be excited to produce electron−hole pairs, while the TiO_2 shell could not be excited, because of its relatively large band gap at 3.16 eV. The major driving force for photogenerated electrons to transfer from the Cu_2O core to the TiO_2 shell is the conduction band offset. A higher CBO value suggested a larger driving force for enhanced charge separation and transfer.

3.5. Surface Photovoltage Spectroscopy (SPS) Analysis Results of Cu_2O@TiO_2 Core−Shell Polyhedra. The surface photovoltage spectroscopy (SPS) measurement is a powerful tool for investigating the photoinduced carrier separation and transfer behavior,[43,44] and the magnitude of SPS response peak is dependent on the amount of net charge accumulated on the material surface.[45] Figure 8 shows the SPS measurement results of pure Cu_2O cuboctahedra and Cu_2O@TiO_2 core−shell polyhedra to compare their photogenerated charge carrier separation efficiencies. It had been reported that the Cu_2O cuboctahedron had a better photocatalytic performance than either the Cu_2O cube or Cu_2O octahedron, because it had better charge carrier separation, because of the different energy levels of its two facets.[46] However, after being coated with TiO_2 to form Cu_2O@TiO_2 heterojunctions, the SPS responses of all three Cu_2O@TiO_2 core−shell polyhedra were enhanced significantly, compared with pure Cu_2O cuboctahedra. This observation suggested that these Cu_2O@TiO_2

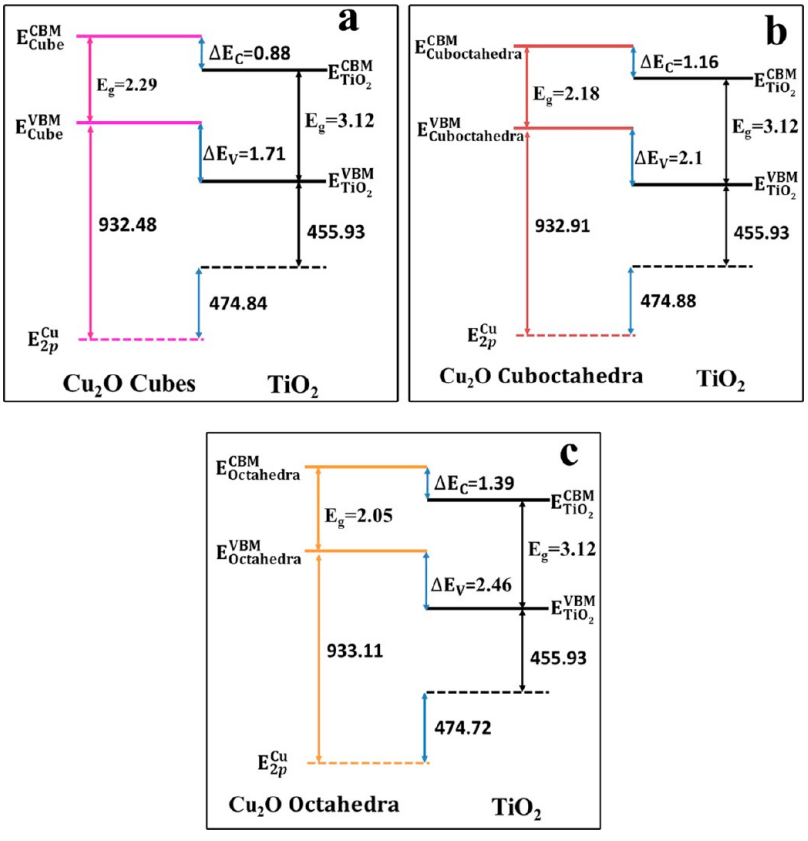

Figure 7. Energy band diagrams of (a) Cu_2O@TiO_2 cubes, (b) Cu_2O@TiO_2 cuboctahedra, and (c) Cu_2O@TiO_2 octahedra.

DOI: 10.1021/am505861c
ACS Appl. Mater. Interfaces 2015, 7, 1465−1476

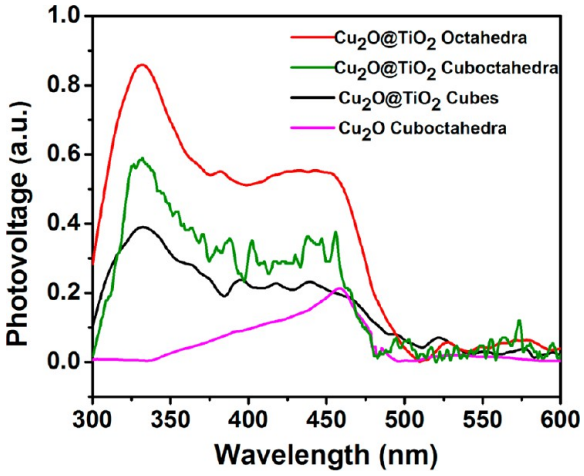

Figure 8. Surface photovoltage spectroscopy (SPS) spectra of Cu_2O@TiO_2 core–shell polyhedra, compared with that of the as-synthesized Cu_2O cuboctahedra.

heterojunction photocatalysts had greatly enhanced charge separation efficiencies, compared to pure Cu_2O under illumination with visible light. As expected, these Cu_2O@TiO_2 core–shell polyhedra showed different SPS response with a clear facet dependency. Cu_2O@TiO_2 octahedra had the strongest SPS response and Cu_2O@TiO_2 cuboctahedra had the medium SPS response, while Cu_2O@TiO_2 cubes had the lowest SPS response. The SPS measurement result was in good agreement with their band offset ranking of these Cu_2O@TiO_2 polyhedra determined by the XPS study. Thus, it could be expected from both the band alignment study and the SPS analysis results that Cu_2O@TiO_2 octahedra should have the best photocatalytic performance among these Cu_2O@TiO_2 core–shell polyhedra and Cu_2O@TiO_2 cuboctahedra should have the medium photocatalytic performance, while Cu_2O@TiO_2 cubes had the lowest photocatalytic performance.

3.6. Photocatalytic Degradation of Methylene Blue and 4-Nitrophenol under Illumination with Visible Light by Cu_2O@TiO_2 Core–Shell Polyhedra and Their Photocatalytic Performance Ranking. The facet-dependent photocatalytic activities of these Cu_2O@TiO_2 core–shell polyhedra were demonstrated by their degradation effect on two model organic contaminants, Methylene Blue (MB) and 4-nitrophenol (4-NP), under illumination with visible light. For comparison purpose, the photocatalytic degradation of MB was also conducted on pure Cu_2O crystals and anatase TiO_2 nanoparticles. Figure 9a summarizes the residue MB percentage versus treatment time under visible-light treatment by these three pure Cu_2O crystals with well-defined facets, compared with that with no photocatalyst presence. Before the illumination with visible light was activated, these photocatalysts were mixed with MB solutions in darkness for an hour to establish the adsorption–desorption equilibrium. When there was no photocatalyst presence, MB solution kept most of its initial concentration under illumination with visible light, and no obvious degradation was observed. The adsorption of MB onto these Cu_2O polyhedra was also examined, which demonstrated that the MB adsorption–desorption equilibrium could be established within an hour and the MB concentration decrease from its adsorption on these Cu_2O polyhedra was only several percent. Under illumination with visible light, these Cu_2O polyhedra demonstrated a photocatalytic degradation

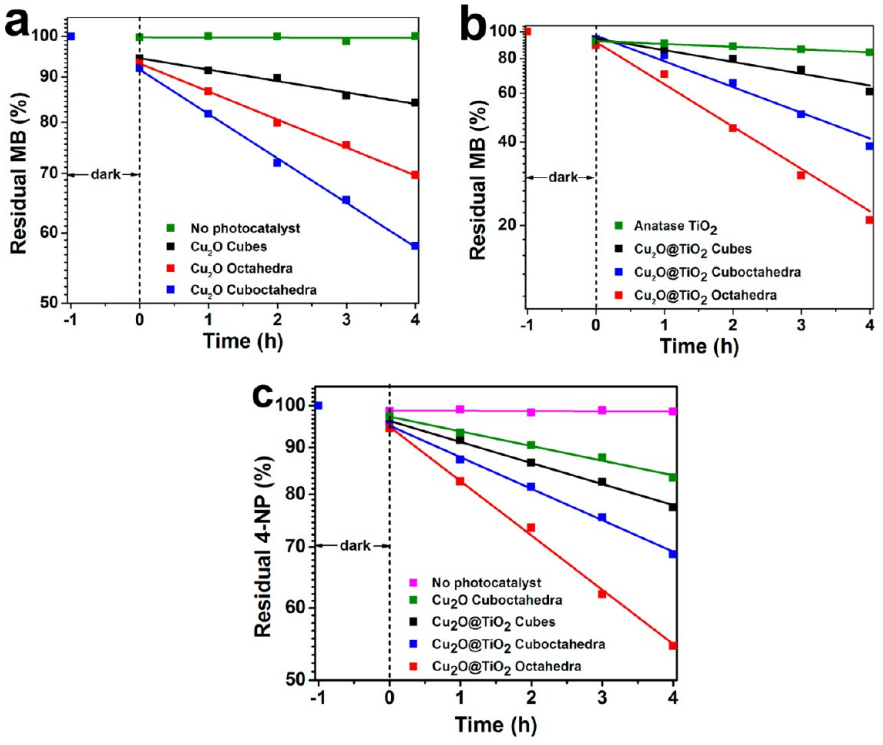

Figure 9. Residual Methylene Blue (MB) percentage versus treatment time under visible-light treatment by (a) Cu_2O crystals with well-defined facets, compared with that with no photocatalyst presence, and (b) Cu_2O@TiO_2 polyhedra, compared with that by anatase TiO_2 nanoparticles. (c) Residual 4-nitrophenol (4-NP) percentage versus treatment time under visible-light treatment by Cu_2O@TiO_2 polyhedra, compared with that by Cu_2O cuboctahedra and that with no photocatalyst presence.

DOI: 10.1021/am505861c
ACS Appl. Mater. Interfaces 2015, 7, 1465–1476

effect on MB, which was in accordance with their visible-light absorption. After 240 min of treatment, the residual MB percentage treated by Cu_2O cubes, Cu_2O cuboctahedra, and Cu_2O octahedra was ~85%, 60%, and 70%, respectively. As expected, the photocatalytic activity of Cu_2O polyhedra was facet-dependent and Cu_2O cuboctahedra exhibited a higher activity than Cu_2O cubes and Cu_2O octahedra, which were in accordance with previous reports.[47] It had been reported that the photocatalytic activity of low-index facets of Cu_2O crystals followed the sequence as {110} > {111} > {100}, which was attributed to the difference on the number and the density per unit surface area of "Cu" dangling bonds on different facets.[24] Thus, Cu_2O octahedra with exposed {111} facets should have a better photocatalytic activity than that of Cu_2O cubes with exposed {100} facets. In Cu_2O cuboctahedra, however, both {100} and {111} facets were exposed. Better charge carrier separation was induced because of the different energy levels of the two facets, and it subsequently resulted in a better photocatalytic activity than that of either Cu_2O cubes or Cu_2O octahedra.[46]

Figure 9b summarizes the residue MB percentage versus treatment time under visible-light treatment by these Cu_2O@TiO_2 polyhedra, compared with that by anatase TiO_2 nanoparticles. Before the visible-light illumination was activated, these photocatalysts were also mixed with MB solutions in darkness for an hour to establish the adsorption−desorption equilibrium. The adsorption of MB onto these Cu_2O@TiO_2 polyhedra or anatase TiO_2 nanoparticles also only caused a decrease of several percent in the MB concentration. Under visible-light illumination, anatase TiO_2 nanoparticles showed very weak MB removal capability. After 240 min of treatment, the residual MB percentage was still ~90%, which could be attributed to their weak photocatalytic activity under visible-light illumination, because of their relatively wide band gap (~3.16 eV). For Cu_2O@TiO_2 polyhedra, they all demonstrated an enhanced photocatalytic degradation effect on MB under illumination with visible light than their counterparts without TiO_2 shells, which could be attributed to the enhanced charge carrier separation by the formation of Cu_2O@TiO_2 $p-n$ heterojunctions. After 240 min of treatment, the residual MB percentages treated by Cu_2O@TiO_2 cubes, Cu_2O@TiO_2 cuboctahedra, and Cu_2O@TiO_2 octahedra were ~60%, 40%, and 20%, respectively.

A first-order exponential decay of the residual MB percentage under illumination with visible light was observed for Cu_2O polyhedra, Cu_2O@TiO_2 polyhedra, and anatase TiO_2 nanoparticles, which could be fitted to eq 5:

$$\mathrm{RP} = a\mathrm{e}^{-bt} \quad (5)$$

where RP is the residue MB percentage, t is the visible-light illumination time, and a and b are the first-order exponential fitting constants. This type of first-order exponential fitting had been observed for various photocatalytic reactions as a characteristic behavior.[48−51] Constant b, which represents the decay rate, could be used as a parameter to compare the photocatalytic degradation efficiency of different photocatalysts. Table 5 summarizes the decay rate values of these photocatalysts on MB degradation under illumination with visible light. As expected, the decay rate of anatase TiO_2 nanoparticles (b = 0.023) was the lowest among these photocatalysts, because of its very weak visible light absorption. The decay rates of Cu_2O cubes, Cu_2O cuboctahedra, and Cu_2O octahedra were determined to be $b \approx$ 0.030, 0.115, and 0.073, respectively. The decay rates of Cu_2O@TiO_2 cubes, Cu_2O@TiO_2 cuboctahedra, and Cu_2O@TiO_2 octahedra were determined at $b \approx$ 0.098, 0.214, and 0.351, respectively, representing increases of ~227%, 86%, and 381%, respectively, over those of their counterparts with no TiO_2 shells.

Table 5. MB Decay Rate Values of Pure Cu_2O Samples, Pure TiO_2 Samples, and Cu_2O@TiO_2 Samples with Heterojunctions on MB Degradation under Illumination with Visible Light

sample	b
Cubic-Cu_2O	0.030
Cubo-Cu_2O	0.115
Octa-Cu_2O	0.073
TiO_2	0.023
Cu_2O@TiO_2 cubes	0.098
Cu_2O@TiO_2 cuboctahedra	0.214
Octa-CT: Cu_2O@TiO_2 octahedra	0.351

It is well-known that MB could absorb visible light and may induce the photosensitization effect. To exclude the photosensitization effect from MB, 4-NP was also used as a target compound to investigated the photocatalytic performance of these Cu_2O@TiO_2 polyhedra. As shown in Figure 9c, the residual 4-NP percentage treated by Cu_2O cuboctahedra after 240 min of treatment was ~85%, while Cu_2O cubes and Cu_2O octahedra showed negligible photocatalytic degradation of 4-NP (not shown in Figure 9c, for the sake of figure clarity). After 240 min of treatment, the residual 4-NP percentages treated by Cu_2O@TiO_2 cubes, Cu_2O@TiO_2 cuboctahedra, and Cu_2O@TiO_2 octahedra were ~80%, 70%, and 50%, respectively, and their corresponding decay rates were determined at ~0.053, 0.080, and 0.137, respectively. The photocatalytic performance ranking of these Cu_2O@TiO_2 polyhedra on the degradation of MB and 4-NP was the same and in accordance with the CBO ranking and SPS analysis results of these Cu_2O@TiO_2 polyhedra, which suggested that the efficient electron−hole pair separation was the key factor to determine their photocatalytic activities.

Interestingly, the photocatalytic performance ranking of Cu_2O@TiO_2 polyhedra was different from that of their counterparts without TiO_2 shells. For pure Cu_2O polyhedra, Cu_2O cuboctahedra had exposed both {100} and {111} facets, which induced the charge carrier separation between {100} and {111} facets.[46] Thus, Cu_2O cuboctahedra had a better photocatalytic activity than that of either Cu_2O cubes with only exposed {100} facets or Cu_2O octahedra with only exposed {111} facets, although {100} facets had a lower photoactivity, compared with {111} facets. However, the introduction of anantase TiO_2 shells created a Cu_2O@TiO_2 $p-n$ heterojunction, which largely affected the charge carrier separation process. The driving force for the charge carrier separation in Cu_2O@TiO_2 polyhedra now was the conduction band offset (CBO) between Cu_2O and TiO_2, not the slight difference in surface energy of the valence and conduction bands between different facets in pure Cu_2O crystals. Heterojunctions constructed on different exposed facets could produce different band alignments, which is also facet-dependent. However, it is not appropriate to assume that a photocatalyst with the favorite exposed facets will still demonstrate the best photocatalytic performance when heterojunctions formed on its exposed facets. The dedicated examination and control of the band alignments formed on

DOI: 10.1021/am505861c
ACS Appl. Mater. Interfaces 2015, 7, 1465−1476

exposed facets are critical for the design of composite photocatalysts with heterojunctions formed on exposed facets in the development of highly efficient photocatalysts.

4. CONCLUSIONS

In summary, Cu_2O@ TiO_2 core−shell structures of cubes, cuboctahedra, and octahedra were created by a carefully controlled hydrolysis of TiF_4 onto Cu_2O crystals with well-controlled morphologies and exposed facets, which demonstrated enhanced photocatalytic performance than pure Cu_2O crystals, because of their better charge carrier separation. Cu_2O@TiO_2 p−n heterojunctions were formed on different exposed Cu_2O facets, and facet-dependent properties were observed. By the combination of optical property measurement and XPS analysis, the energy band alignments of these Cu_2O@ TiO_2 polyhedra were determined, which provided the insight into the understanding of the photocatalytic performance differences among these Cu_2O@TiO_2 core−shell polyhedra. SPS analysis results also confirmed the relatively photocatalytic activity ranking of these Cu_2O@TiO_2 core−shell polyhedra. Under illumination with visible light, Cu_2O@TiO_2 octahedra demonstrated the best photocatalytic performance on MB and 4-NP degradations, because of their highest conduction band offset, followed by Cu_2O@TiO_2 cuboctahedra and Cu_2O@ TiO_2 cubes. The photocatalytic performance ranking of Cu_2O@TiO_2 polyhedra was different with that of pure Cu_2O polyhedra without TiO_2 shells, which could be attributed to the different driving forces for the charge carrier separation. This study demonstrated that the dedicated examination and control of the band alignments formed on exposed facets are critical for the design of composite photocatalysts with heterojunctions formed on exposed facets, which provides a new prospect in the development of highly efficient photocatalysts for a broad range of applications.

AUTHOR INFORMATION

Corresponding Author

*Tel.: +86-24-83978028. Fax: +86-24-23971215. Postal address: 72 Wenhua Road, Shenyang 110016, Liaoning Province, PRC. E-mail address: qili@imr.ac.cn (Q. Li).

Notes

The authors declare no competing financial interest.

ACKNOWLEDGMENTS

This study was supported by the National Natural Science Foundation of China (Grant No. 51102246), the Knowledge Innovation Program of Institute of Metal Research, Chinese Academy of Sciences (Grant No. Y0N5A111A1), the Youth Innovation Promotion Association, Chinese Academy of Sciences (Grant No.Y2N5711171), and the Scientific Research Foundation for the Returned Overseas Chinese Scholars, State Education Ministry, P. R. China.

REFERENCES

(1) Fujishima, A.; Honda, K. Electrochemical Photolysis of Water at a Semiconductor Electrode. *Nature* **1972**, *238*, 37−38.

(2) Hoffmann, M. R.; Martin, S. T.; Choi, W.; Bahnemann, D. W. Environmental Applications of Semiconductor Photocatalysis. *Chem. Rev.* **1995**, *95*, 69−96.

(3) Ochiai, T.; Fujishima, A. Photoelectrochemical Properties of TiO_2 Photocatalyst and its Applications for Environmental Purification. *J. Photochem. Photobiol., C* **2012**, *13*, 247−262.

(4) Chatterjee, D.; Dasgupta, S. Visible Light Induced Photocatalytic Degradation of Organic Pollutants. *J. Photochem. Photobiol., C* **2005**, *6*, 186−205.

(5) Daghrir, R.; Drogui, P.; Robert, D. Modified TiO_2 for Environmental Photocatalytic Applications: A Review. *Ind. Eng. Chem. Res.* **2013**, *52*, 3581−3599.

(6) Liu, G.; Wang, L.; Yang, H. G.; Cheng, H.-M.; Lu, G. Q. Titania-based Photocatalysts—Crystal Growth, Doping and Heterostructuring. *J. Mater. Chem.* **2010**, *20*, 831.

(7) Dai, G.; Yu, J.; Liu, G. Synthesis and Enhanced Visible-Light Photoelectrocatalytic Activity of p−n Junction BiOI/TiO_2 Nanotube Arrays. *J. Phys. Chem. C* **2011**, *115*, 7339−7346.

(8) Su, D.; Wang, J.; Tang, Y.; Liu, C.; Liu, L.; Han, X. Constructing WO_3/TiO_2 Composite Structure towards Sufficient Use of Solar Energy. *Chem. Commun.* **2011**, *47*, 4231−4233.

(9) Li, Q.; Li, Y. W.; Wu, P.; Xie, R.; Shang, J. K. Palladium Oxide Nanoparticles on Nitrogen-Doped Titanium Oxide: Accelerated Photocatalytic Disinfection and Post-Illumination Catalytic "Memory". *Adv. Mater.* **2008**, *20*, 3717−3723.

(10) Wang, H.; Zhang, L.; Chen, Z.; Hu, J.; Li, S.; Wang, Z.; Liu, J.; Wang, X. Semiconductor Heterojunction Photocatalysts: Design, Construction, and Photocatalytic Performances. *Chem. Soc. Rev.* **2014**, *43*, 5234−5244.

(11) Iliev, V.; Tomova, D.; Bilyarska, L.; Eliyas, A.; Petrov, L. Photocatalytic Properties of TiO_2 Modified with Platinum and Silver Nanoparticles in the Degradation of Oxalic Acid in Aqueous Solution. *Appl. Catal., B* **2006**, *63*, 266−271.

(12) Yang, H. G.; Sun, C. H.; Qiao, S. Z.; Zou, J.; Liu, G.; Smith, S. C.; Cheng, H. M.; Lu, G. Q. Anatase TiO_2 Single Crystals with a Large Percentage of Reactive Facets. *Nature* **2008**, *453*, 638−641.

(13) Rawalekar, S.; Mokari, T. Rational Design of Hybrid Nanostructures for Advanced Photocatalysis. *Adv. Energy Mater.* **2013**, *3*, 12−27.

(14) Liu, G.; Yu, J. C.; Lu, G. Q.; Cheng, H. M. Crystal Facet Engineering of Semiconductor Photocatalysts: Motivations, Advances and Unique Properties. *Chem. Commun.* **2011**, *47*, 6763−6783.

(15) Huang, M. H.; Rej, S.; Hsu, S. C. Facet-dependent Properties of Polyhedral Nanocrystals. *Chem. Commun.* **2014**, *50*, 1634−1644.

(16) Yang, H.; Liu, G.; Qiao, S.; Sun, C.; Jin, Y.; Smith, S.; Zou, J.; Cheng, H.; Lu, G. Solvothermal Synthesis and Photoreactivity of Anatase TiO_2 Nanosheets with Dominant {001} Facets. *J. Am. Chem. Soc.* **2009**, *131*, 4078−4083.

(17) Shi, W.; Yang, W.; Li, Q.; Gao, S.; Shang, P.; Shang, J. The Synthesis of Nitrogen/sulfur Co-doped TiO_2 Nanocrystals with a High Specific Surface Area and a High Percentage of {001} Facets and their Enhanced Visible-light Photocatalytic Performance. *Nanoscale Res. Lett.* **2012**, *7*, 590.

(18) Li, N.; Liu, M.; Zhou, Z.; Zhou, J.; Sun, Y.; Guo, L. Charge Separation in Facet-Engineered Chalcogenide Photocatalyst: A Selective Photocorrosion Approach. *Nanoscale* **2014**, *6*, 9695−9702.

(19) Zhao, X.; Jin, W.; Cai, J.; Ye, J.; Li, Z.; Ma, Y.; Xie, J.; Qi, L. Shape- and Size-Controlled Synthesis of Uniform Anatase TiO_2 Nanocuboids Enclosed by Active {100} and {001} Facets. *Adv. Funct. Mater.* **2011**, *21*, 3554−3563.

(20) Ohno, T.; Sarukawa, K.; Matsumura, M. Crystal Faces of Rutile and Anatase TiO_2 Particles and Their Roles in Photocatalytic Reactions. *New J. Chem.* **2002**, *26*, 1167−1170.

(21) Yanina, S. V.; Rosso, K. M. Linked Reactivity at Mineral−Water Interfaces through Bulk Crystal Conduction. *Science* **2008**, *320*, 218−222.

(22) Li, R.; Zhang, F.; Wang, D.; Yang, J.; Li, M.; Zhu, J.; Zhou, X.; Han, H.; Li, C. Spatial Separation of Photogenerated Electrons and Holes among {010} and {110} Crystal Facets of $BiVO_4$. *Nat. Commun.* **2013**, *4*, 1432.

(23) Ho, J. Y.; Huang, M. H. Synthesis of Submicrometer-Sized Cu_2O Crystals with Morphological Evolution from Cubic to Hexapod Structures and Their Comparative Photocatalytic Activity. *J. Phys. Chem. C* **2009**, *113*, 14159−14164.

DOI: 10.1021/am505861c
ACS Appl. Mater. Interfaces 2015, 7, 1465−1476

(24) Zhang, Y.; Deng, B.; Zhang, T.; Gao, D.; Xu, A.-W. Shape Effects of Cu_2O Polyhedral Microcrystals on Photocatalytic Activity. *J. Phys. Chem. C* **2010**, *114*, 5073−5079.
(25) Sui, Y.; Fu, W.; Yang, H.; Zeng, Y.; Zhang, Y.; Zhao, Q.; Li, Y.; Zhou, X.; Leng, Y.; Li, M.; Zou, G. Low Temperature Synthesis of Cu_2O Crystals: Shape Evolution and Growth Mechanism. *Cryst. Growth Des.* **2010**, *10*, 99−108.
(26) Shi, H.; Yu, K.; Sun, F.; Zhu, Z. Controllable Synthesis of Novel Cu_2O Micro/nano-crystals and Their Photoluminescence, Photocatalytic and Field Emission Properties. *CrystEngComm* **2012**, *14*, 278.
(27) Zhang, Y.-G.; Ma, L.-L.; Li, J.-L.; Yu, Y. In Situ Fenton Reagent Generated from TiO_2/Cu_2O Composite Film: A New Way to Utilize TiO_2 under Visible Light Irradiation. *Environ. Sci. Technol.* **2007**, *41*, 6264−6269.
(28) Qiu, X.; Miyauchi, M.; Sunada, K.; Minoshima, M.; Liu, M.; Lu, Y.; Li, D.; Shimodaira, Y.; Hosogi, Y.; Kuroda, Y.; Hashimoto, K. Hybrid Cu_xO/TiO_2 Nanocomposites As Risk-Reduction Materials in Indoor Environments. *ACS Nano* **2011**, *6*, 1609−1618.
(29) Huang, L.; Peng, F.; Wang, H.; Yu, H.; Li, Z. Preparation and Characterization of Cu_2O/TiO_2 Nano−Nano Heterostructure Photocatalysts. *Catal. Commun.* **2009**, *10*, 1839−1843.
(30) Liu, L.; Yang, W.; Li, Q.; Gao, S.; Shang, J. K. Synthesis of Cu_2O Nanospheres Decorated with TiO_2 Nanoislands, Their Enhanced Photoactivity and Stability under Visible Light Illumination, and Their Post-illumination Catalytic Memory. *ACS Appl. Mater. Interfaces* **2014**, *6*, 5629−5639.
(31) Zhang, D. F.; Zhang, H.; Guo, L.; Zheng, K.; Han, X. D.; Zhang, Z. Delicate Control of Crystallographic Facet-Oriented Cu_2O Nanocrystals and the Correlated Adsorption Ability. *J. Mater. Chem.* **2009**, *19*, 5220.
(32) Yanhong, L.; Dejun, W.; Qidong, Z.; Min, Y.; Qinglin, Z. A Study of Quantum Confinement Properties of Photogenerated Charges in ZnO Nanoparticles by Surface Photovoltage Spectroscopy. *J. Phys. Chem. B* **2004**, *108*, 3202−3206.
(33) Yang, L.; Luo, S.; Li, Y.; Xiao, Y.; Kang, Q.; Cai, Q. High Efficient Photocatalytic Degradation of *p*-Nitrophenol on a Unique Cu_2O/TiO_2 *p*−*n* Heterojunction Network Catalyst. *Environ. Sci. Technol.* **2010**, *44*, 7641−7646.
(34) Chu, S.; Zheng, X.; Kong, F.; Wu, G.; Luo, L.; Guo, Y.; Liu, H.; Wang, Y.; Yu, H.; Zou, Z. Architecture of $Cu_2O@TiO_2$ Core−Shell Heterojunction and Photodegradation for 4-Nitrophenol under Simulated Sunlight Irradiation. *Mater. Chem. Phys.* **2011**, *129*, 1184−1188.
(35) Wang, Z.; Lou, X. W. TiO_2 Nanocages: Fast Synthesis, Interior Functionalization and Improved Lithium Storage Properties. *Adv. Mater.* **2012**, *24*, 4124−4129.
(36) Tauc, J.; Grigorovici, R.; Vancu, A. Optical Properties and Electronic Structure of Amorphous Germanium. *Phys. Status Solidi B* **1966**, *15*, 627−637.
(37) Uddin, M. T.; Nicolas, Y.; Olivier, C.; Toupance, T.; Servant, L.; Muller, M. M.; Kleebe, H. J.; Ziegler, J.; Jaegermann, W. Nanostructured SnO_2−ZnO Heterojunction Photocatalysts Showing Enhanced Photocatalytic Activity for the Degradation of Organic Dyes. *Inorg. Chem.* **2012**, *51*, 7764−7773.
(38) Ng, C. H. B.; Fan, W. Y. Shape Evolution of Cu_2O Nanostructures via Kinetic and Thermodynamic Controlled Growth. *J. Phys. Chem. B* **2006**, *110*, 20801−20807.
(39) Asahi, R.; Morikawa, T.; Ohwaki, T.; Aoki, K.; Taga, Y. Visible-light Photocatalysis in Nitrogen-doped Titanium Oxides. *Science* **2001**, *293*, 269−271.
(40) Owen, M. H. S.; Guo, C.; Chen, S.-H.; Wan, C. T.; Cheng, C. C.; Wu, C. H.; Ko, C. H.; Wann, C. H.; Ivana; Zhang, Z.; Sheng Pan, J.; Yeo, Y. C. Band Alignment Study of Lattice-Matched InAlP and Ge Using X-ray Photoelectron Spectroscopy. *Appl. Phys. Lett.* **2013**, *103*, 031604.
(41) Kramm, B.; Laufer, A.; Reppin, D.; Kronenberger, A.; Hering, P.; Polity, A.; Meyer, B. K. The Band Alignment of Cu_2O/ZnO and Cu_2O/GaN Heterostructures. *Appl. Phys. Lett.* **2012**, *100*, 094102.
(42) Kraut, E. A.; Grant, R. W.; Waldrop, J. R.; Kowalczyk, S. P. Precise Determination of the Valence-Band Edge in X-Ray Photoemission Spectra: Application to Measurement of Semiconductor Interface Potentials. *Phys. Rev. Lett.* **1980**, *44*, 1620−1623.
(43) Kronik, L.; Shapira, Y. Surface Photovoltage Phenomena: Theory, Experiment, and Applications. *Surf. Sci. Rep.* **1999**, *37*, 1−206.
(44) Duzhko, V.; Timoshenko, V. Y.; Koch, F.; Dittrich, T. Photovoltage in Nanocrystalline Porous TiO_2. *Phys. Rev. B* **2001**, *64*, 075204.
(45) Zhang, Q.; Wang, D.; Xu, J.; Cao, J.; Sun, J.; Wang, M. An Investigation of Surface Photovoltaic Properties of TiOPc and AlClPc. *Mater. Chem. Phys.* **2003**, *82*, 525−528.
(46) Zhang, L.; Shi, J.; Liu, M.; Jing, D.; Guo, L. Photocatalytic Reforming of Glucose under Visible Light over Morphology Controlled Cu_2O: Efficient Charge Separation by Crystal Facet Engineering. *Chem. Commun.* **2014**, *50*, 192−194.
(47) Huang, W. C.; Lyu, L. M.; Yang, Y. C.; Huang, M. H. Synthesis of Cu_2O Nanocrystals from Cubic to Rhombic Dodecahedral Structures and Their Comparative Photocatalytic Activity. *J. Am. Chem. Soc.* **2012**, *134*, 1261−1267.
(48) Liu, H.; Cheng, S.; Zhang, J.; Cao, C.; Zhang, S. Titanium Dioxide as Photocatalyst on Porous Nickel: Adsorption and the Photocatalytic Degradation of Sulfosalicylic Acid. *Chemosphere* **1999**, *38*, 283−292.
(49) Dionysiou, D. D.; Khodadoust, A. P.; Kern, A. M.; Suidan, M. T.; Baudin, I.; Laine, J. M. Continuous-mode Photocatalytic Degradation of Chlorinated Phenols and Pesticides in Water Using a Bench-scale TiO_2 Rotating Disk Reactor. *Appl. Catal., B* **2000**, *24*, 139−155.
(50) Domenech, X.; Peral, J. Kinetics of the Photocatalytic Oxidation of N(III) and S(IV) on Different Semiconductor Oxides. *Chemosphere* **1999**, *38*, 1265−1271.
(51) Leng, W. H.; Liu, H.; Cheng, S. A.; Zhang, J.; Cao, C. Kinetics of Photocatalytic Degradation of Aniline in Water over TiO_2 Supported on Porous Nickel. *J. Photochem. Photobiol., A* **2000**, *131*, 125−132.

DOI: 10.1021/am505861c
ACS Appl. Mater. Interfaces 2015, 7, 1465−1476